

Modelling the bicycle rider as a controller

Literature Review

C. Christoforidis



MODELLING THE BICYCLE RIDER AS A CONTROLLER

LITERATURE REVIEW

by

C. Christoforidis

in partial fulfillment of the requirements for the degree of

Master of Science
in Biomedical Engineering

at the Delft University of Technology.

Student number: 4737822
Project duration: 2018 – 2019
Supervisor: Dr. ir. A.L. Schwab, TU Delft
Thesis committee: Dr. ir. R. Happee, TU Delft
MSc. G. Dialynas, TU Delft

This thesis is confidential and cannot be made public until May, 2019.

©2019
C. Christoforidis

ALL RIGHTS RESERVED An electronic version of this thesis is available at
<http://repository.tudelft.nl/>.

ABSTRACT

Bicycle riding is a fundamental part of everyday transportation in many countries around the world. Ever since the development of the safety bicycle, the bicycle remains one of the most prominent means of transport. Despite cycling's prominence in every day life for almost two centuries we still do not fully understand how the rider controls the bike in a more systematic way.

The purpose of this literature study is to explore and evaluate models of the single track vehicle rider found in the researched bibliography. Firstly a brief analysis of bicycle stability and its dynamics is presented as explored by Meijaard et al.[9]. In Chapter 3models which were classified on their control theory approach are presented. In section ??, models using the classical control approach are described. Following the steps of early cybernetics research in which airplane pilot modelling was pioneered by McRuer[6–8], a plethora of authors attempted adapting McRuers crossover model in order to model the rider of a seemingly much more complex task, motorcycle and bicycle riding. However some argued that such an approach will not work since cycling is not just a compensatory task. These spawned a new wave of research focusing in optimal control which is described in section ?? . This approach has its roots in early motor control research in which the human brain is believed to work as a constrained optimal controller. In the final section of Chapter 3, all models that do not fall under the two approaches described above are reviewed. These include fuzzy logic controllers which have the advantage of incorporating heuristic findings that are impossible to formulate using systematic mathematical approaches. Also intermittent control is briefly explored as a solution.

Based on this literature review the graduation project will try to model the human controller for bicycles, while focusing on the roll stabilization task. Open road experiments will be conducted in effort to estimate the controller's parameters and indirectly validate it with real cycling data.

*C. Christoforidis
Delft, April 2018*

CONTENTS

1	Introduction	1
2	Methods	3
2.1	Bicycle dynamics and stability	3
2.1.1	The linearized Whipple-Carvalho bicycle model	3
2.1.2	The linearized equations of motion	4
2.2	The Delft steer-by-wire bicycle	6
2.3	Estimation of Rider Torque	7
2.3.1	Steer rate and acceleration	9
2.3.2	Steering shaft moment of inertia and viscous friction	9
2.3.3	Motor Torque Input Validation	11
2.4	Roll Angle Estimation	14
3	Results	17
4	Conclusions	19
A	Calibration of Inertial Measurements	21
B	Orientation Estimation from Inertial Measurements	25
B.1	Offline Estimation Methods	25
B.2	Online Estimation Methods	26
	Bibliography	31

1

INTRODUCTION

Bicycle riding is a fundamental part of everyday transportation in many countries around the world. Ever since the development of the safety bicycle(two equal sized wheels, pneumatic tires, chain drive, rear wheel propulsion and a bent front fork), almost 130 years ago, the bicycle remains one of the most prominent means of transport [4]. With the growing concerns of sedentary lifestyles many choose the bicycle as their primary commute vehicle with the hopes of maintaining some levels of fitness. Additionally the bicycle is the preferred means of physical exercise for the elderly especially in the Netherlands and Denmark. Despite the fact that riding a bicycle is one of the first skills we acquire as kids and is used throughout the adult life, the fundamental way humans control the bicycle and ,generally single track vehicles, is yet to be understood.

In a recent study examining the entries of patients to the emergency department due to traffic related accidents in the Netherlands (see Fig. 2.8), it was found that bicycle related accidents were the most prevalent. With over 60,000 reported cases bicycle accidents outnumber automobile accidents more than 4 to 1. It therefore becomes clear that a lot could be done to improve cycling safety. Further look at the figure will reveal that most of those accidents did not involve a second party. There was just a rider that fell off his bike. Although there are several potential reasons that riders lose control of the bicycle, formulating a general model of how humans control single track vehicles could prove invaluable in understanding the causes behind the above numbers.

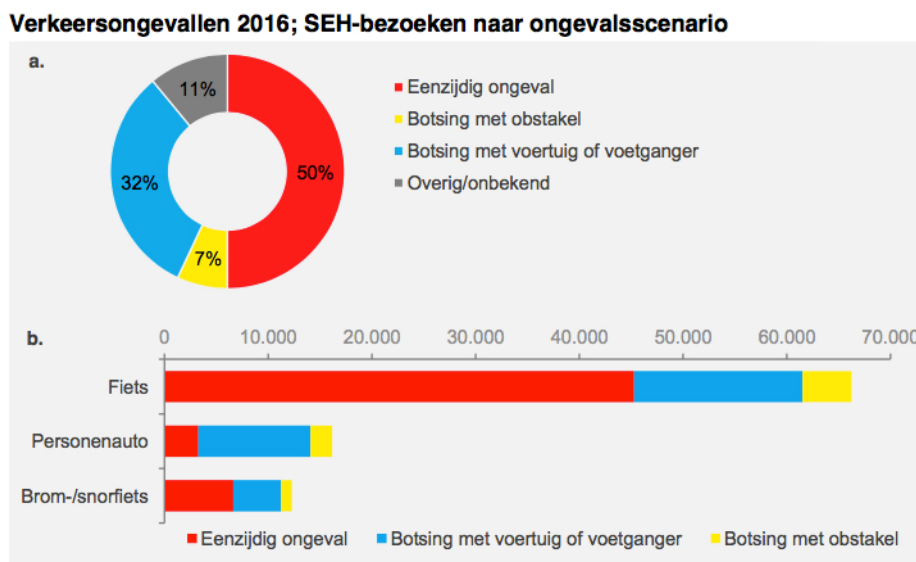


Figure 1.1: The number of road users that visit the emergency department at a hospital after a traffic accident in the Netherlands in 2016. Red indicates single vehicle accidents, yellow indicates a collision with an obstacle, blue indicates multi-vehicle accident and grey indicates other type of accidents[5].

Every human-machine system requires an understanding of how the plant operates. In the case of the bicycle multiple efforts have been made in capturing the dynamics of the bicycle and its self-stabilizing behavior. These have resulted in a set of linearized equations of motion, now commonly referred to as the Whipple Carvalho model [9], which is going to be discussed further in chapter 3.

As it is known single track vehicles are not stable at low speeds. This is why a controller (like the human rider) is required to close the loop and create a stable system. There are two ways with which the human affects the dynamics of the plant. The first is with its passive interactions with the plant as a physical multi-body system. Most passive models model the rider as a point mass rigidly attached to the rear frame, or as a pendulum connected to the rear frame [2], although recent efforts have been made to extend this further with more complex passive rider models which include modeling of neuromuscular dynamics with spring-damper systems at various interfaces between rider and the bicycle frame[3]. The second is with its active control behavior. This involves the active control motion, such as steering, leaning or pedaling, applied by the rider to control and balance the bicycle. In most such cases, the passive behavior of the rider is simplified by only accounting for a fixed mass on the seat post, but when lean torque needs to be examined more complex modeling is required. The focus of the study is to explore the available models that best express the human rider as a controller in the bicycle-rider closed loop system.

The literature review presented herein gives an overview of research done in the field of active rider modelling concerning single-track vehicles, while discussing with which methods and to what extent have these models been validated. This extensive overview is given in section ?? of chapter 3, which is structured in three sections: ?? Classical control system design, ?? Optimal control system design and ?? Other control system design. Chapter 4 concludes on the results from Chapter 3 having as a final goal to answer the research question:

- **What is the controller that best simulates the behavior of the human in the control of single track vehicles?**

2

METHODS

2.1. BICYCLE DYNAMICS AND STABILITY

Bicycles are very reliable transport vehicles and are considered the most efficient man powered form of transportation. Since the inception of the safety bicycle not much has changed with regards to the design of the two wheeled vehicle. Bicycle design has been based on tinkering rather than equations which has resulted in little mathematical scrutiny in the available bicycle analyses. When trying to design a controller for a bicycle, a model that accurately describes its dynamics and kinematics is required but until 2007 there was no consensus on a set of equations that do that, so research on rider control for bicycles was hardly attempted. This changed when Meijaard et al.[9] developed a set of linearized equations of motion for the Whipple-Carvalho bicycle model (fig 2.1).

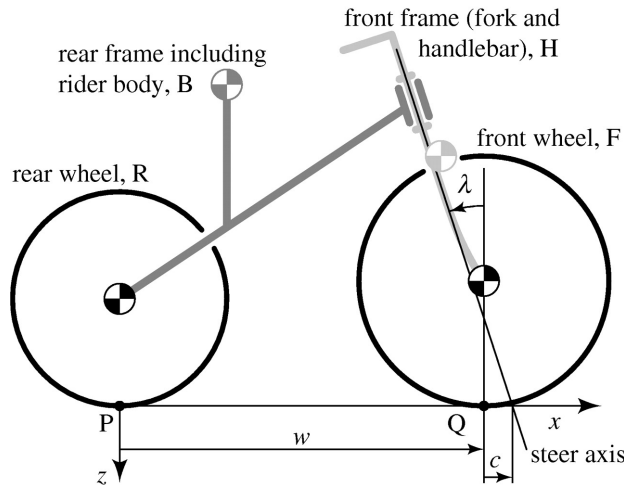


Figure 2.1: The Whipple-Carvalho bicycle model consists of four rigid bodies: rear wheel R, rear frame B, front frame H and front wheel F connected via hinges. The center of mass locations are expressed relative to the x - and z -coordinates shown (with origin at P and y pointing towards the reader). The other parameters shown are the steer axis tilt λ , wheelbase w and trail c . The model at its most expanded form is described by 25 parameters.[9]

2.1.1. THE LINEARIZED WHIPPLE-CARVALHO BICYCLE MODEL

For the equations of motion to be derived several assumptions were made by Meijaard et al.[9]:

1. The rider is rigidly connected to the rear frame with the mass of the arms included in the mass.
2. The contact between tire and ground is modelled as a non-slipping rolling point-contact, meaning that wheels have an ideal rotation without lateral slip.
3. Friction between moving parts and pedaling forces is neglected. Thus, the total energy of the system is

constant.

4. The bicycle is moving with constant forward velocity.

In order to understand the derived equations of motion a consideration must be made with regards to the configuration space and the velocity space of the model. The benchmark bicycle model derived is defined by 25 parameters. However, as a result of holonomic constraints (hinges and ground contacts) and non-holonomic constraints (non-slipping rolling contacts), its accessible configuration space can be reduced to 7 parameters. Coordinates x_P and y_P represent the translational position of the rear wheel point P, δ is the steer angle, θ_F and θ_R are the front and rear wheel angles respectively. Finally ϕ represents the lean angle about the x axis while ψ represents the yaw rotation about the z axis. All this is depicted in figure 2.9.

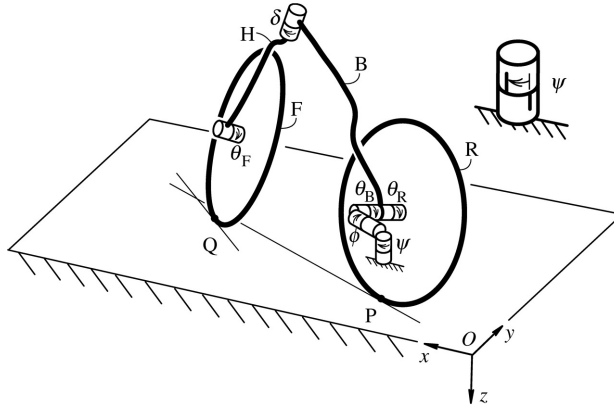


Figure 2.2: Depiction of the benchmark bicycle in 3D. The cans represent a hinge between two rigid bodies. Multiple cans in series denote multiple degrees of freedom and the order of rotation.[9]

As it turns out some of the configuration variables do not appear in any of the equations of motion of the different parts. These so-called cyclic or ignorable coordinates are: the location of the bicycle on the plane (x_P , y_P), the heading of the bicycle ψ and the rotations (θ_R , θ_F) of the two wheels relative to their respective frames [9]. Additionally due to a symmetry of the bicycle design and the lateral equations of motion, a first order decoupling between forward and lateral dynamics exists [9]. This means that the equations governing forward movement can be ignored when examining lateral dynamics like bicycle stabilization and vice versa. In conclusion, the three independent degrees of freedom that define the equations of motion are the forward speed v , the lean angle ϕ and the steering angle δ (figure 2.9).

2.1.2. THE LINEARIZED EQUATIONS OF MOTION

Keeping in mind the above considerations Meijaard et al.[9] managed to formulate a set of three linearized equations that each describe a degree of freedom. The first is a first order differential equation that describes the forward speed as shown in equation 2.1[9].

$$\left[r_R^2 m_T + I_{Ryy} + \left(\frac{r_R}{r_F} \right)^2 I_{Fyy} \right] \ddot{\theta}_R = T_{\theta_R} \quad (2.1)$$

where I , r and m denote inertia, radius and mass respectively of the rigid body defined in the subscript. Also T_{θ_R} denotes the torque applied to the rear wheel in the direction of θ_R .

For the two remaining degrees of freedom the lean angle(ϕ) and the steer angle (δ) they found two second-order differential equations that are coupled and are given by equation 2.2[9].

$$\mathbf{M}\ddot{\mathbf{q}} + v\mathbf{C}_1\dot{\mathbf{q}} + [g\mathbf{K}_0 + v^2\mathbf{K}_2]\mathbf{q} = \mathbf{f} \quad (2.2)$$

where \mathbf{q} is a vector containing the roll and steer angles, \mathbf{f} is a vector containing the roll and steer torques, g is the gravitational acceleration and \mathbf{M} , $v\mathbf{C}_1$, $g\mathbf{K}_0 + v^2\mathbf{K}_2$ are the "mass", "damping" and "stiffness" ratios in matrix form respectively.

When talking about bicycle stability and control, equation 2.1 is often ignored as the task of pedaling is often removed from the problem so as to focus on pure roll stabilization. For control purposes it is convenient to

express the bicycle equation 2.2 in state-space form . The state-space representation is:

$$\dot{\mathbf{x}} = \mathbf{Ax} + \mathbf{Bf} \quad (2.3)$$

$$\mathbf{y} = \mathbf{Cx} + \mathbf{Df} \quad (2.4)$$

where matrices A, B, C, D are defined by:

$$\mathbf{A} = \begin{bmatrix} -\mathbf{M}^{-1}\nu\mathbf{C}_1 & -\mathbf{M}^{-1}(g\mathbf{K}_0 + \nu^2\mathbf{K}_2) \\ \mathbf{I} & \mathbf{0} \end{bmatrix}, \mathbf{B} = \begin{bmatrix} \mathbf{M}^{-1} \\ \mathbf{0} \end{bmatrix}, \mathbf{C} = [\mathbf{0} \quad \mathbf{I}], \mathbf{D} = [\mathbf{0}] \quad (2.5)$$

By finding the eigenvalues of matrix A one can begin asking questions regarding the stability of the system. Meijaard et al. [9] found the eigenvalues for different forwards speeds and managed to determine the region in which the uncontrolled benchmark bicycle was stable. In figure 2.10 the four eigenvalues are plotted in a forward speed range $0 < \nu < 10 \text{ ms}^{-1}$. The region that is defined when the real part of the weave eigenvalue becomes negative and the capsize eigenvalue has not crossed the zero threshold yet is the stable region and corresponds to forward speeds $4.3 \lesssim \nu \lesssim 6 \text{ ms}^{-1}$. When designing a controller the input signals f are tasked with influencing the poles of the characteristic polynomial and moving the system from the unstable region to a stable one.

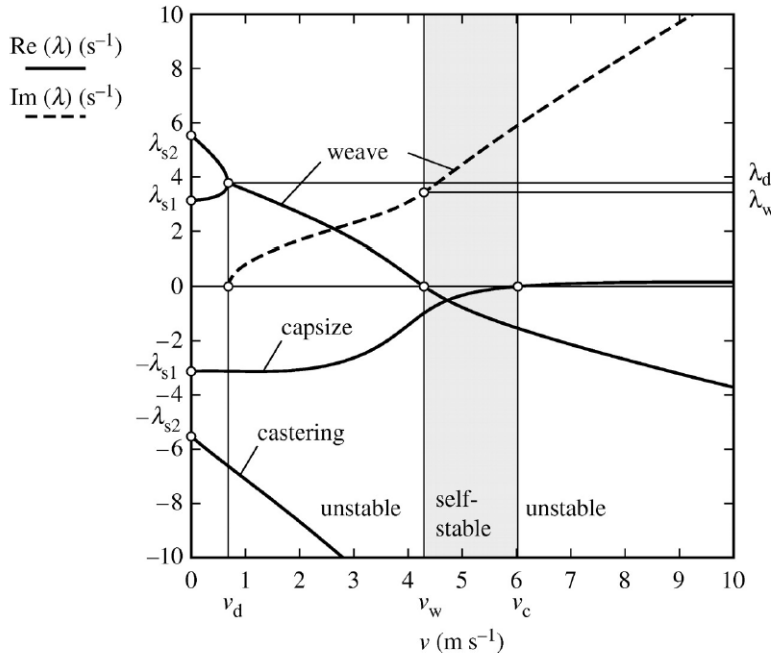


Figure 2.3: Root locus plot of the benchmark bicycle. Bold black lines indicate the real part of the eigenvalues while dotted show the imaginary part.[9]

Before exploring potential control options for the bicycle model described by the above equations, it is interesting to see to what extent is the model controllable. We know that the bicycles and motorcycles are controllable in reality but how well does this model capture reality is still a question.

To determine controllability of a dynamical system the reachability matrix :

$$\mathbf{Q} = [\mathbf{B}, \mathbf{AB}, \mathbf{A}^2\mathbf{B}, \dots, \mathbf{A}^{k-1}\mathbf{B}] \quad (2.6)$$

must be full rank. When the matrix rank is equal to the number of states of the system then the system is controllable by inputs f . By taking the determinant and then solving the equation:

$$\det \mathbf{Q} = 0 \quad (2.7)$$

the forward velocities that result in an uncontrollable system can be found. Schwab et al. in [11] isolated the control inputs and found that a Whipple like bicycle with the an extended rider model can be controlled by either lean or steer torque for the practical range of 1 to $10 \frac{m}{s}$. Although some forward speeds that result in a zero determinant exist they were either extremely close to zero or part of a stable mode so they concluded that they are of no concern.

2.2. THE DELFT STEER-BY-WIRE BICYCLE

An instrumented steer-by-wire bicycle was recently developed by Delft's Bicycle Lab [1]. Steer-by-wire is a technology where electronic sensors and actuators are used to replace conventional mechanical systems. In this case the mechanical link between the handlebar and the fork was removed. This bicycle was the core tool used for the experimental process as it proved to be a versatile platform for rider control identification.

By removing the mechanical link an additional degree of freedom in the Whipple model is added, the fork angle θ . In order to simulate normal bicycle dynamics a controller is needed that will close the margin between steer angle δ and angle θ . This was achieved by the use of a PD-controller of the following form:

$$\begin{aligned} T_{PDH} &= K_{PH}(\delta - \theta) + K_{DH}(\dot{\delta} - \dot{\theta}) \\ T_{PDF} &= K_{PF}(\delta - \theta) + K_{DF}(\dot{\delta} - \dot{\theta}) \end{aligned} \quad (2.8)$$

where T_{PDH} is the torque applied by the handlebar motor, T_{PDF} is the torque applied by the fork motor and $K_{PH}, K_{PF}, K_{DH}, K_{DF}$ are the proportional and differential gains respectively. The updated input to the system is given by:

$$\bar{\mathbf{f}} = \begin{bmatrix} T_\delta \\ T_\phi \\ T_\theta \end{bmatrix} = \begin{bmatrix} T_H - T_{PDH} \\ T_\phi \\ T_{PDF} \end{bmatrix} \quad (2.9)$$

where T_H is the torque applied by the rider.

Using the parameters of table 2.1 the matrices of equation 2.2 are calculated for the steer-by-wire bicycle (see APPENDIX for full discription). Doing the root locus analysis for the updated bicycle model the stable speed region can be calculated. The stable region corresponds to speeds $4.39 \lesssim v \lesssim 6.67 \text{ ms}^{-1}$ (see Fig. 2.4).

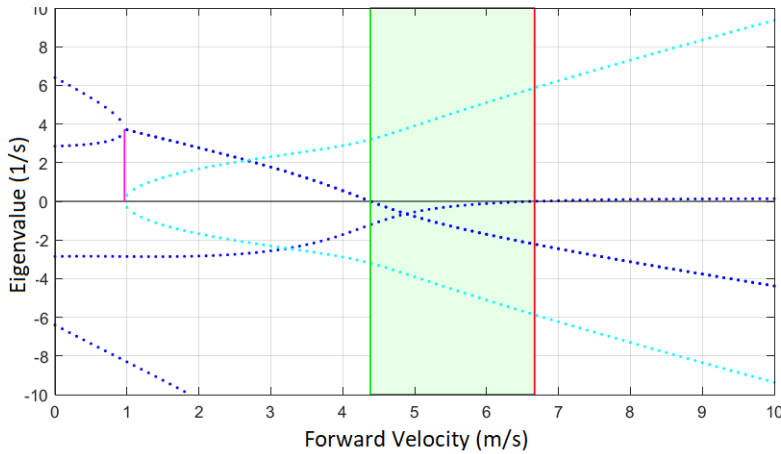


Figure 2.4: Root locus plot of the steer by wire bicycle. Dotted blue lines indicate the real part of the eigenvalues while dotted cyan show the imaginary part.

The bicycle has an inertia measurment unit (IMU MPU9250) that measures roll, pitch and yaw rate as well as linear accelerations. The IMU is located and oriented as shown in figure 2.5. It also has two rotary encoders; one in the back wheel to measure forward speed (v) and one in the pedal to measure pedal cadence. Angle encoders measure the angles δ and θ for the controller to function. A torque sensor was also custom made and placed in the handlebar assembly. Its purpose was to validate that the command torque to the motor is equal to the torque applied by the motor. For more regarding the torque sensor see section 2.3.3. Finally the bike has a rear wheel motor so a constant speed can be easily set and the pedalling task is removed from

the problem. For certain necessary signals, such as roll angle and input torque, no direct measurement from sensors were available so these signals were estimated using the methods described below.



Figure 2.5: The steer-by-wire bicycle with the locations of all its sensors. The axis indicate the orientation of measurements for the IMU sensor.

2.3. ESTIMATION OF RIDER TORQUE

Given the steer rate ($\dot{\delta}$) and acceleration ($\ddot{\delta}$), moment of inertia (I_H), motor damping (b_m) and the torque applied by the handlebar motor (T_{PDH}) the equation of motion of the upper handlebar assembly can be formed (see Fig. 2.6) and solved for the unknown rider input torque (T_H).

$$T_H = \ddot{\delta} I_H + \dot{\delta} b_m - T_{PDH} \quad (2.10)$$

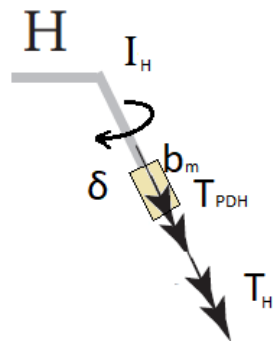


Figure 2.6: Free body diagram of the upper handlebar assembly.

Parameter	Symbol	Value
wheel base	w	$1.03m$
trail	c	$0.0665m$
steer axis tilt ($\pi/2 - \text{head angle}$)	λ	$\pi/10$
rear wheel	R	
radius	r_R	$0.6858m$
mass	m_R	$8.5\ kg$
mass moment of inertia	$(I_{R_{xx}}, I_{R_{yy}})$	$(0.095625, 0.19125)\ kg\ m^2$
rear body and frame assembly	B	
position centre of mass	(x_B, z_B)	$(0.4, -0.6)$
mass	m_B	$95kg$
mass moment of inertia	$\begin{bmatrix} I_{B_{xx}} & 0 & I_{B_{xz}} \\ 0 & I_{B_{yy}} & 0 \\ I_{B_{xz}} & 0 & I_{B_{zz}} \end{bmatrix}$	$\begin{bmatrix} 9.2 & 0 & 2.4 \\ 0 & 11 & 0 \\ 2.4 & 0 & 2.8 \end{bmatrix}\ kg\ m^2$
front handlebar and fork assembly	H	
position centre of mass	(x_H, z_H)	$(0.9, -0.66)$
mass	m_H	$1.5kg$
mass moment of inertia	$\begin{bmatrix} I_{H_{xx}} & 0 & I_{H_{xz}} \\ 0 & I_{H_{yy}} & 0 \\ I_{H_{xz}} & 0 & I_{H_{zz}} \end{bmatrix}$	$\begin{bmatrix} 0.05892 & 0 & -0.00756 \\ 0 & 0.06 & 0 \\ -0.00756 & 0 & 0.00708 \end{bmatrix}\ kg\ m^2$
front wheel	F	
radius	r_F	$0.6858m$
mass	m_F	$1.84kg$
mass moment of inertia	$(I_{F_{xx}}, I_{F_{yy}})$	$(0.097, 0.195)\ kg\ m^2$
battery rack	b	
position centre of mass	(x_b, z_b)	$(0.4, -0.55)$
mass	m_b	$4kg$
mass moment of inertia	$\begin{bmatrix} I_{H_{xx}} & 0 & I_{H_{xz}} \\ 0 & I_{H_{yy}} & 0 \\ I_{H_{xz}} & 0 & I_{H_{zz}} \end{bmatrix}$	$\begin{bmatrix} 0.02 & 0 & -0.02 \\ 0 & 0.04 & 0 \\ -0.02 & 0 & 0.02 \end{bmatrix}\ kg\ m^2$

Table 2.1: Whipple model parameters for the steer-by-wire bicycle shown in figure 2.5.

2.3.1. STEER RATE AND ACCELERATION

Since only the steering angle is directly measurable, a way needs to be found that produces accurate estimations of steer rate and steer acceleration. Simple numerical differencing techniques proved ineffective as noise effects were magnified resulting in corrupted second derivatives, even after filtering the original signal to a cutoff frequency of 10 Hz.

To combat this problem a piecewise cubic interpolation technique using the cubic spline function was used. The principle of this method is simple. Third order polynomials are fitted between the datapoints. This results in a signal that is identical to the original but instead of discrete points, it is represented by the union of polynomial functions. After this point the steer rate and acceleration can be easily obtained by taking the derivatives of the polynomials. the result of the method is seen in figure 2.7.

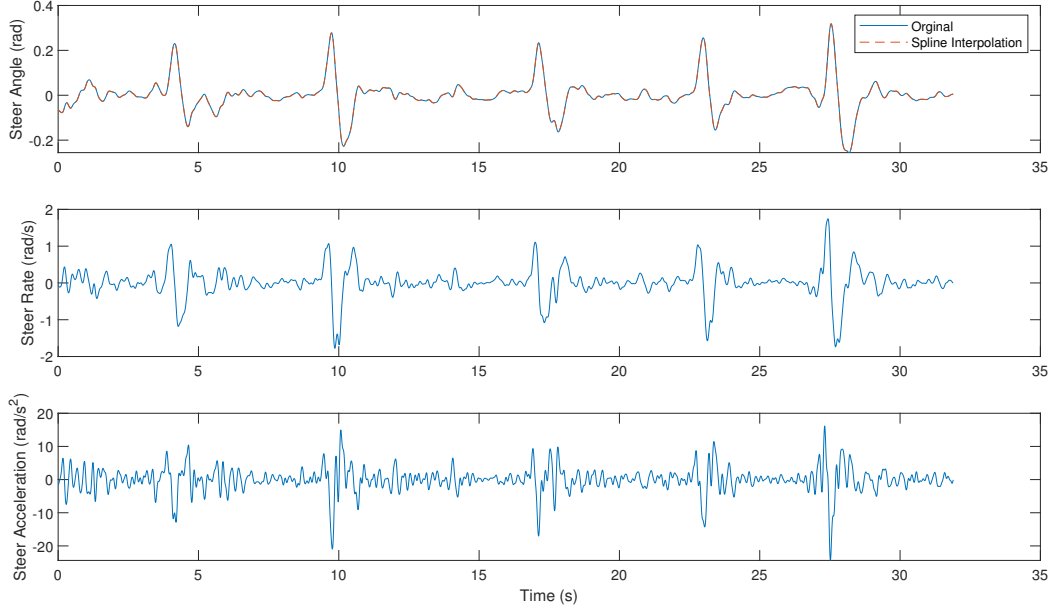


Figure 2.7: Steering angle signal with its derivates produced by the piecewise cubic spline interpolation method.

2.3.2. STEERING SHAFT MOMENT OF INERTIA AND VISCOUS FRICTION

In order to make estimation of applied rider torque, the damping coefficient and the inertia of the steering shaft needs to be determined. There are multiple ways to measure inertia of complex geometries. Here an estimation through a simple experimental setup is chosen.

By connecting the steering shaft with two extension springs (see Fig.2.8) and measuring the oscillations of the steering angle δ , a mechanical system is created where it has to obey equation 2.11.

$$I_H \ddot{\delta}(t) + b_m \dot{\delta}(t) + 2K\alpha^2 \delta(t) = 0 \quad (2.11)$$

where K the spring elastic constant and α the moment arm shown in figure 2.8.

The springs ($K = 555 \text{ N/m}$ and slack length of 0.03 m) are attached to the handlebar and the system is perturbed. The measured steering angle signal from one of the perturbation tests is shown in figure 2.9. The steering rate and acceleration signals are derived by the methods described in section 2.3.1. Equation 2.11 is then applied to all discrete time steps and so the system of equations 2.12 is created.

$$\begin{bmatrix} \ddot{\delta}_1 & \dot{\delta}_1 \\ \ddot{\delta}_2 & \dot{\delta}_2 \\ \vdots & \vdots \\ \ddot{\delta}_N & \dot{\delta}_N \end{bmatrix} \begin{bmatrix} I_H \\ b_m \end{bmatrix} = -2K\alpha^2 \begin{bmatrix} \delta_1 \\ \vdots \\ \delta_N \end{bmatrix} \quad (2.12)$$

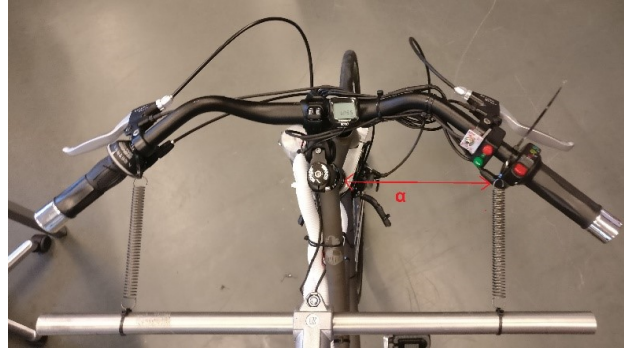


Figure 2.8: Spring-handlebar assembly where α is the moment arm.

where N the length of the recorded signal.

Since equation 2.12 is linear in the parameters, the solution of the regression problem can be approximated by the use of the least squares method.

$$\begin{bmatrix} I_H \\ b_m \end{bmatrix} = -2K\alpha^2 \left(\begin{bmatrix} \ddot{\delta}_1 & \dot{\delta}_1 \\ \ddot{\delta}_2 & \dot{\delta}_2 \\ \vdots & \vdots \\ \ddot{\delta}_N & \dot{\delta}_N \end{bmatrix}^T \begin{bmatrix} \ddot{\delta}_1 & \dot{\delta}_1 \\ \ddot{\delta}_2 & \dot{\delta}_2 \\ \vdots & \vdots \\ \ddot{\delta}_N & \dot{\delta}_N \end{bmatrix} \right)^{-1} \begin{bmatrix} \ddot{\delta}_1 & \dot{\delta}_1 \\ \ddot{\delta}_2 & \dot{\delta}_2 \\ \vdots & \vdots \\ \ddot{\delta}_N & \dot{\delta}_N \end{bmatrix}^T \begin{bmatrix} \delta_1 \\ \delta_2 \\ \vdots \\ \delta_N \end{bmatrix} \quad (2.13)$$

The system is perturbed 15 times so 15 sets of inertia and damping ratios are computed. The mean of the these was taken and resulted in $I_H = \mathbf{0.0960 \text{ kg m}^2}$ and $b_m = \mathbf{0.2663 \text{ N s}^{-1}}$

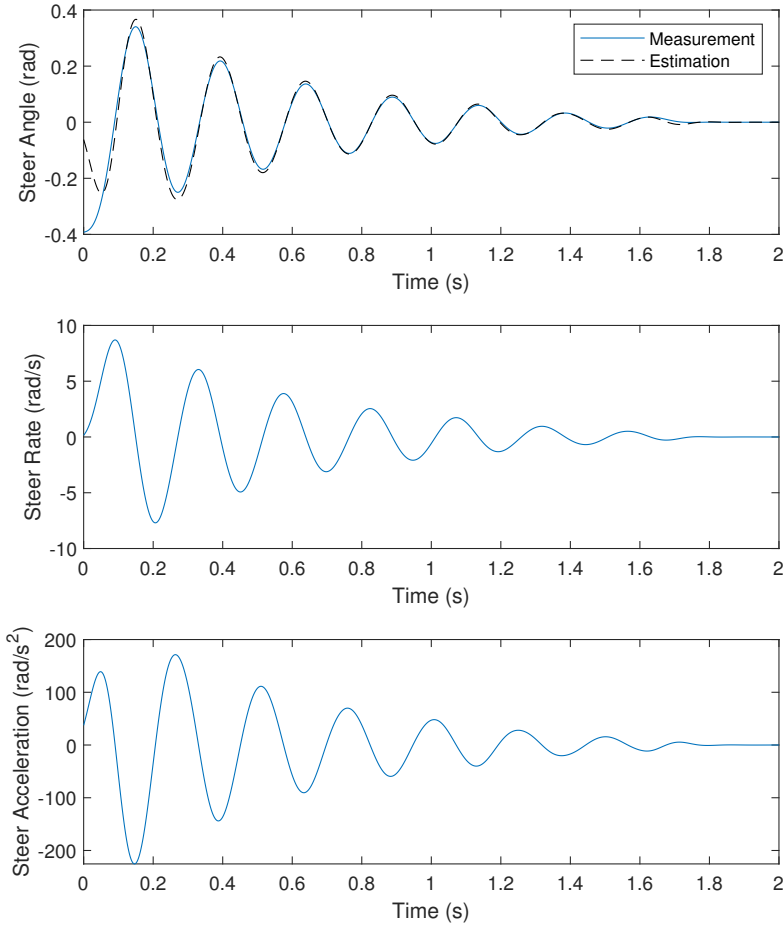


Figure 2.9: Result of the first of fifteen oscillations. Blue lines indicate the measured signals while the black dotted line is the output of the model given the values of inertia and damping estimated with the least squares method.

2.3.3. MOTOR TORQUE INPUT VALIDATION

DESIGN OF TORQUE SENSOR

In order to validate that the torque exerted by the handlebar motor results in equivalent input rider torque a torque sensor is designed and attached to the steering shaft. The most common torque sensor measurement principle uses bonded strain gauge technology, where the strain gauges are bonded to a suitably designed shaft.

In the torsion of a cylindrical shaft the strain is measured by the angle of twist or angular deflection. Unfortunately stain gauges can only detect compressive and tensile strain. The strain gauges are placed with such an orientation that the shearing stress is replaced by its equivalent principal stresses. The angle and the magnitude of the principal stresses are calculated by the use of the Mohr Circle. In this case the principal tension and compressive stresses are of the same magnitude as the shearing stress and are active at an angle of 45 degrees since it is considered that no external compressive or tension force is present.

In order to design a proper cylindrical shaft for the torque sensor the diameter of the shaft is chosen such that the strain measured in the strain gauges is within the detectable range ($\epsilon_{min} = 10^{-5}$, $\epsilon_{max} = 6 \cdot 10^{-4}$). For this application, a hollow cylindrical shaft made of aluminum (AL7075 – O) is used so the unknowns are the inner and outer diameters. The strain is given in relation to the stress by Hooke's law for isotropic materials by equation (2.14). The shearing stress is in turn given by equation (2.15).

$$\epsilon = \frac{\sigma \cdot (1 + \nu)}{E} \quad (2.14)$$

where ν the Poisson's ratio and E the Young's Modulus (Pa)

$$\tau = \frac{T \cdot r}{J} \quad (2.15)$$

where J is the polar moment of inertia (m^4), r the distance from center to stressed surface in the given position (mm), T the twisting moment (Nm). The polar moment of inertia of a circular hollow shaft can be expressed as

$$J = \frac{\pi \cdot (D^4 - d^4)}{32} \quad (2.16)$$

where d is shaft inside diameter (mm) and D is the shaft outside diameter (mm).

By inputting the above equations into a MATLAB script figure 2.10 was produced. The figure was created for a fixed inner diameter of 12mm, due to limitations in the machining process. It is evident that the lower the width of the shaft the higher detection of the low level torques. For this reason a width of 2 mm was chosen. This still means that torques below 0.2Nm are not detectable. However the purpose of the torque sensor is not to provide accurate online measurements but to validate the input torques from the handlebar motor. The design of the resulting part is shown in 2.11.

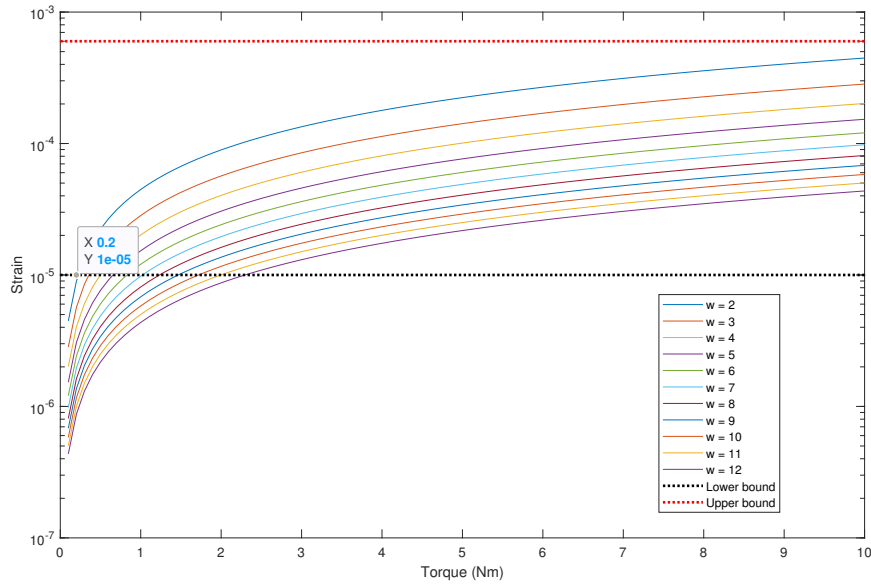


Figure 2.10: Principal tensile strain in the 45 degree angle for various shaft widths (w).

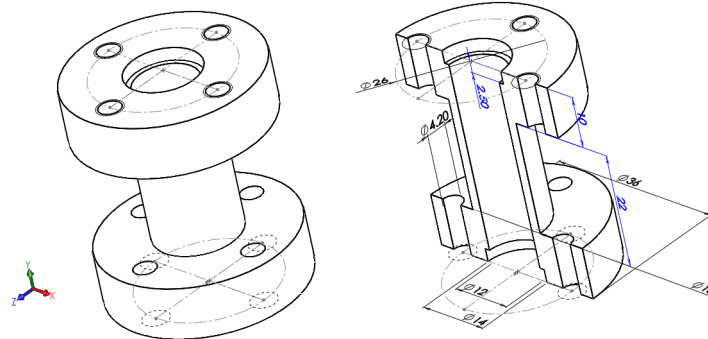
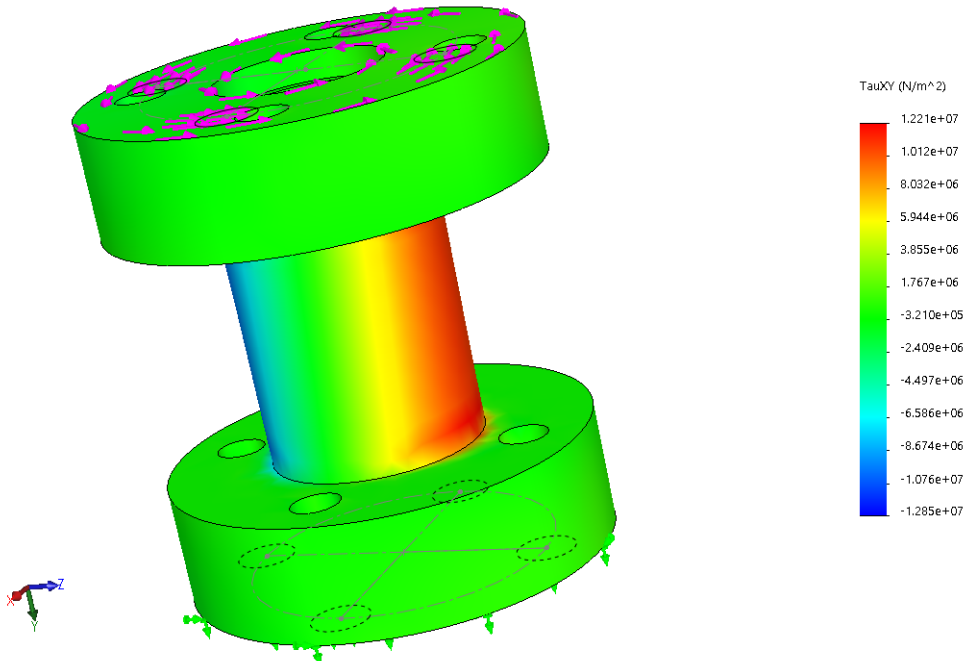


Figure 2.11: Schematic of the hollow shaft.

Because it is not an ideal hollow cylinder, the shearing stress calculated analytically from the above equations needs to be validated. A static load simulation in SolidWorks is done to see how much different is the shearing stress on the external surface. As it turns out the simulation showed a shearing stress similar to the one calculated by the equations. In 2.12 the simulation results for a loading of $10Nm$ is shown. For comparison the resulting shearing stress calculated analytically is $10.0874 \cdot 10^6 N/m^2$. For proper measurements of strain the gauge placement should gravitate towards the middle to avoid the spikes of shearing stress near the intersections between the main shaft and the cylindrical heads (see fig. 2.12)

Figure 2.12: Shearing stress for $10Nm$ loading in the axial direction.

RESULTS

In order to validate that the commanded torque in the handlebar motor is the same as the one actually applied in the handlebar, a trial identification run was conducted to simulate steer torque levels of the experiments. The signal of the input motor torque is compared with the output of the custom made torque sensor. The results are shown in figure 2.13. The mismatch of the two signals for values lower than $0.5Nm$ is attributed to the fact that the sensor's strain gauges cannot accurately measure the strain in the material to produce reliable output as determined analytically beforehand. Also during the measurements a slight bias

of the sensor was noted when $0 < \delta < \pi/2$. Despite the aforementioned, the resulting Variance Accounted For (VAF) was equal to 90.77% and was deemed that the motor command torque is indeed what is being applied in the steering shaft so in all subsequent calculation it was taken as ground truth.

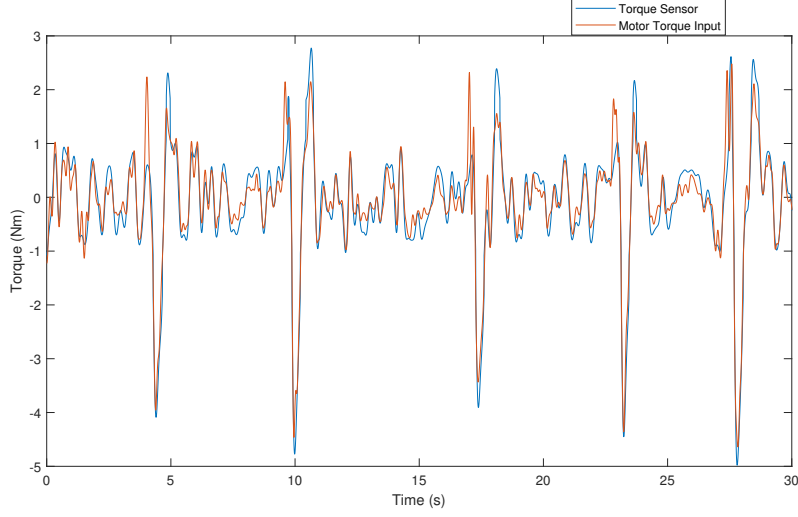


Figure 2.13: Measurement of torque sensor compared to the commanded torque of the handlebar motor.

2.4. ROLL ANGLE ESTIMATION

The need for reliable and accurate measurements of roll angle are paramount. Unfortunately, the steer-by-wire bike does not have sensor that can directly produce measurements of roll angle. For this reason an indirect approach is used that was developed by Sanjurjo et al. [10]. The method produces satisfactory roll angle estimations using only the angular rates measured by an IMU sensor.

Kalman filters are often used as state estimators when multiple measurement sources need to be combined into a single more reliable one. Often the output of a model is combined with absolute measurements and an estimation of the state is made by dynamically weighting the two sources of information. In this case a simple plant model is created which has the roll rate from the IMU as input and produces the roll angle of the next time step given the previous one. In order to account for biases in the angular rate sensor an extra state b_x is added to the model. The complete formulation is given by :

$$\begin{bmatrix} \hat{\phi} \\ \hat{b}_x \end{bmatrix}_k^- = \begin{bmatrix} 1 & -dt \\ 0 & 1 \end{bmatrix} \begin{bmatrix} \hat{\phi} \\ \hat{b}_x \end{bmatrix}_{k-1}^+ + \begin{bmatrix} dt \\ 0 \end{bmatrix} \omega_x^B \quad (2.17)$$

where ω_x^B is the angular rate IMU measurement in the x direction (see Fig.2.5), k indicates the current time step and dt is the time step.

In the correction stage of the Kalman filter absolute measurements of the roll angle are needed, but such measurements are not available. For this reason equations 2.18 and 2.19 are used as pseudo absolute measurements. Sanjuro et al. explain that equation 2.18 is more reliable for roll angles close to zero and equation 2.19 is more reliable for larger roll angles, for this reason a weighted sum of the two methods is employed 2.20 that follows the weighting function 2.21 .

$$\phi_d = \arctan\left(\frac{\omega_z^B v}{g}\right) \quad (2.18)$$

$$\phi_w = \arctan\left(\frac{\omega_y^B}{\omega_z^B}\right) \quad (2.19)$$

$$\phi_m = W\phi_d + (1 - W)\phi_w \quad (2.20)$$

$$W = \exp\left(-\frac{\hat{\phi}^2}{\phi^2}\right) \quad (2.21)$$

where ω_y^B, ω_z^B are the angular rate IMU measurements in the y and z direction respectively (see Fig.2.5), W is the weighting function $\hat{\phi}$ is the last available estimation of roll and $\bar{\phi}^2$ is a constant that can be used to adjust the weighting function. In [10] Sanjuro et al. used $\bar{\phi}^2 = 0.05$.

The method was used in a trial rider identification run to test if it can estimate the ranges of roll angle sway present during the experiments. The output is seen in figure 2.14. From the result it is evident that the pseudo-absolute measurements are quite noisy. For this reason emphasis was focused on the model by tuning the initial values of covariance of the model state estimation to be much lower than that of the measurements.

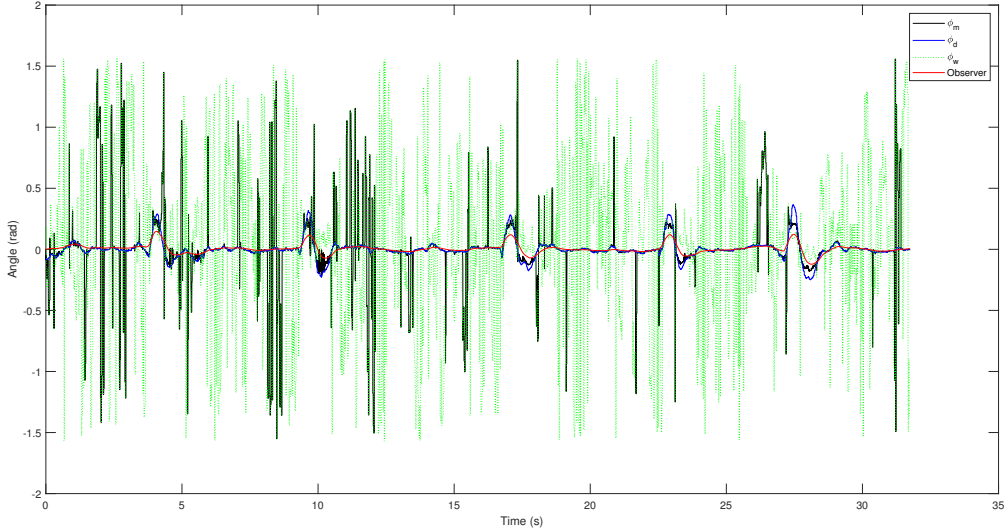


Figure 2.14: Roll angle estimation output from the trial run. The red line indicates the final ouput of the kalman filter.

3

RESULTS

4

CONCLUSIONS

A

CALIBRATION OF INERTIAL MEASUREMENTS

The fixed body angular velocities measured by the Inertial Measurement Unit (IMU) are biased due the imperfect orientation of the sensor axis (see figure A.1). The goal is it to align system xyz with the global coordinate system XYZ. To achieve this the euler angle offsets are calculated by using the measurements from MPU-9050's built in accelerometer.



Figure A.1: Bicycle with body fixed sensor axis x-y-z (B) and global axis XYZ (G).

Different orders of rotation affects the end configuration. For this study the intrinsic order Z-Y'-X'' is adopted which is equivalent to the extrinsic X-Y-Z (roll-pitch-yaw). The inverse rotation matrix that described the above rotation sequence is :

$$R_{xyz} = R_x(\phi)R_y(\theta)R_z(\psi) = \begin{pmatrix} \cos\theta \cos\psi & \cos\theta \sin\psi & -\sin\theta \\ \cos\psi \sin\theta \sin\phi - \cos\phi \sin\psi & \cos\phi \cos\psi + \sin\theta \sin\phi \sin\psi & \cos\theta \sin\phi \\ \cos\phi \cos\psi \sin\theta + \sin\phi \sin\psi & \cos\phi \sin\theta \sin\psi - \cos\psi \sin\phi & \cos\theta \cos\phi \end{pmatrix} \quad (\text{A.1})$$

(a) Configuration $i = 1$ (b) Configuration $i = 2$

Figure A.2: a) The bicycle's desired Z axis is aligned with the vector of gravitational acceleration. The bike was validated to be completely upright by the use of a calibrated commercial IMU (MTw Awinda). b) The bicycle's desired X axis is aligned with the vector of gravitational acceleration. The door was validated to be completely vertical by the use of a calibrated commercial IMU (MTw Awinda). \mathbf{g} is the vector measured by the accelerometer which opposite to the gravitational acceleration.

where ϕ is the angle of rotation around axis X, θ is the angle of rotation around axis Y and ψ is the angle of rotation around axis Z. Equation (A.1) maps a vector from the global system G to the body fixed system B. In order to estimate the euler angle offsets the bike was configured in two different ways to align the gravity vector with the z and x axis respectively. The readings from the accelerometer are expressed in the sensor frame (B). Equation (A.2) is used to solve for the euler angle offsets. Unfortunately the three equations have only two degrees of freedom so two configurations are required so as to solve for all three angles.

In the first, $i = 1$ and $\mathbf{g}_1 = [0 \ 0 \ 1]^T$ (see figure A.2a) (note that the vector of accelerations is normalized) with equation (A.2) solving for θ and ϕ . The lack of any dependence on the yaw angle is intuitive to understand since a rotation around the z-axis is aligned with the gravitational field and accelerometers are completely insensitive to rotations about the gravitational field vector. Consequently in the second, $i = 2$ and $\mathbf{g}_2 = [-1 \ 0 \ 0]^T$ which leads to equation (A.2) solving for ψ and θ (see figure A.2b).

$$\frac{\mathbf{G}_i^B}{\|\mathbf{G}_i^B\|} = \begin{pmatrix} G_{ix}^B \\ G_{iy}^B \\ G_{iz}^B \end{pmatrix} \frac{1}{\sqrt{G_{ix}^{B^2} + G_{iy}^{B^2} + G_{iz}^{B^2}}} = \mathbf{R}_{xyz(\phi_o, \theta_o, \psi_o)} \mathbf{g}_i \quad (\text{A.2})$$

Solving equation (A.2) for the angles we get :

$$\phi_o = \tan^{-1} \left(\frac{G_{1y}^B}{G_{1z}^B} \right) \quad (\text{A.3})$$

$$\theta_o = \tan^{-1} \left(\frac{G_{1x}^B}{\sqrt{G_{1y}^B{}^2 + G_{1z}^B{}^2}} \right) \quad (\text{A.4})$$

$$\psi_o = \tan^{-1} \left(\frac{-G_{2y}^B}{\sqrt{G_{2x}^B{}^2 + G_{2z}^B{}^2}} \right) \quad (\text{A.5})$$

From equations (A.3) to (A.5) the euler angle offsets calculated are inserted into rotation matrix R_{xyz} . The transpose of the result (A.6) is then used to transform the IMU measurements from the coordinate frame B to the coordinate frame G which is consistent with the linearized equations of motion defined in section 2.1.2.

$$R_{IMU} = R_{xyz}^T(\phi_o, \theta_o, \psi_o) = \begin{pmatrix} 0.9939 & -0.006106 & -0.1105 \\ 0.006069 & 1.0 & -0.000675 \\ 0.1105 & 0 & 0.9939 \end{pmatrix} \quad (\text{A.6})$$

B

ORIENTATION ESTIMATION FROM INERTIAL MEASUREMENTS

In order to properly assess the state of the bicycle when comparing it with the Whipple model, measurements of roll angle ϕ and yaw angle ψ are necessary. However the steer-by-wire bicycle has no way of measuring either. For this reason an estimation method is required that can approximate these angles by using measurements from already existing Inertial sensors. A distinction is made between methods that can estimate the euler angles when the whole signal is available for processing and for methods that can produce real-time estimation.

B.1. OFFLINE ESTIMATION METHODS

An estimation of the roll and yaw angle can be made by using the angular rates measured by the gyroscope. However euler angle rates and angular velocities are not equivalent as the former are dependant on order of rotation while the latter are a vector expressed in the body frame. For this reason an expression needs to be formulated that connects the two. Since the euler angle rates are expressed in the local frame of that particular rotation sequence, appropriate rotation matrices need to be used to transform them into vectors in the final body fixed frame (B). The order of rotation used here is the intrinsic X-Y'-Z" (roll-pitch-yaw).

$$\begin{pmatrix} {}^B\omega_x \\ {}^B\omega_y \\ {}^B\omega_z \end{pmatrix} = \begin{pmatrix} 0 \\ 0 \\ \psi \end{pmatrix} + {}^B R_G \begin{pmatrix} 0 \\ \dot{\theta} \\ 0 \end{pmatrix} + {}^B R_G {}^G R_F \begin{pmatrix} \dot{\phi} \\ 0 \\ 0 \end{pmatrix} \quad (\text{B.1})$$

where ${}^B\omega_x, {}^B\omega_y, {}^B\omega_z$ the angular rates measured by the gyroscope and F, G the local coordinate systems after the first and second rotation respectively. Note that these measurements are corrected for the imperfect orientation of the IMU sensor by transforming with matrix R_{IMU} (see equation (A.6))

$$\begin{pmatrix} {}^B\omega_x \\ {}^B\omega_y \\ {}^B\omega_z \end{pmatrix} = \begin{pmatrix} 1 & 0 & -\sin\theta \\ 0 & \cos\phi & \cos\theta \sin\phi \\ 0 & -\sin\phi & \cos\phi \cos\theta \end{pmatrix} \begin{pmatrix} \dot{\phi} \\ \dot{\theta} \\ \dot{\psi} \end{pmatrix} \quad (\text{B.2})$$

Simply solving equation (B.2) for the euler angle rates yields the expressions that can be used to calculate the roll and yaw rates from gyroscope measurements.

$$\dot{\phi} = ({}^B\omega_y \sin\phi + {}^B\omega_z \cos\phi) \tan\theta + {}^B\omega_x \approx {}^B\omega_x \quad (\text{B.3})$$

$$\dot{\psi} = \frac{{}^B\omega_y \sin\phi + {}^B\omega_z \cos\phi}{\cos\theta} \approx {}^B\omega_y \sin\phi + {}^B\omega_z \cos\phi \quad (\text{B.4})$$

The newly calculated euler angle rate signals can now be numerically integrated to produce the corresponding euler angles. However, a way needs to be found to account for the accumulating integration error. When the whole signal is available, which is true only in offline (post-processing) applications, two methods were tested for approximating euler angles. The first method removes the drift simply through the use of a high-pass filter. All frequency content under 0.05 Hz is filtered. The second method, removes the drift by subtracting the resulting line from a linear regression. Worth noting here that for the yaw angle this will produce good approximations only when the median of the true signal is around zero, which was mostly true since the subjects tried to keep straight heading in order to avoid falling outside the boundaries of the bicycle lane. For the roll angle this assumptions is confidently made since the signal is expected to be centered around zero. The disadvantage of the high-pass filter was that magnitudes of signals are slightly attenuated, while the disadvantage of the linear regression detrending is that a bias can be introduced if the median is not zero.

B.2. ONLINE ESTIMATION METHODS

With no prior knowledge of the resulting drift another method needs to be found to correct the integration output. Fortunately there are existing ways with which two unreliable sources of a signal can be combined in order to produce a more reliable one. For this a secondary source of pseudo measurements is needed.

My first naive implementation was to calculate the roll from the accelerometer data by assuming that gravity is the only force captured in the accelerometer readings. The formulation of the estimators is identical to the equation (A.3). However, this is not ideal for the particular application of single track vehicles since lateral accelerations due to centrifugal forces heavily change the accelerometer measurements.

Sanjurjo et al. [10] used equations B.5 and B.6 as pseudo absolute measurements. Note that B.6 is directly derived from the second equation of B.2. They explain that equation B.5 is more reliable for angles close to zero and equation B.6 is more reliable for larger roll angles, for this reason a weighted sum of the two methods is employed B.7 that follows the weighting function B.8 .

$$\phi_d = \tan^{-1} \left(\frac{\omega_z^B v}{g} \right) \quad (\text{B.5})$$

$$\phi_\omega = \tan^{-1} \left(\frac{\omega_y^B}{\omega_z^B} \right) \quad (\text{B.6})$$

$$\phi_m = W\phi_d + (1 - W)\phi_\omega \quad (\text{B.7})$$

$$W = \exp \left(-\frac{\hat{\phi}^2}{\bar{\phi}^2} \right) \quad (\text{B.8})$$

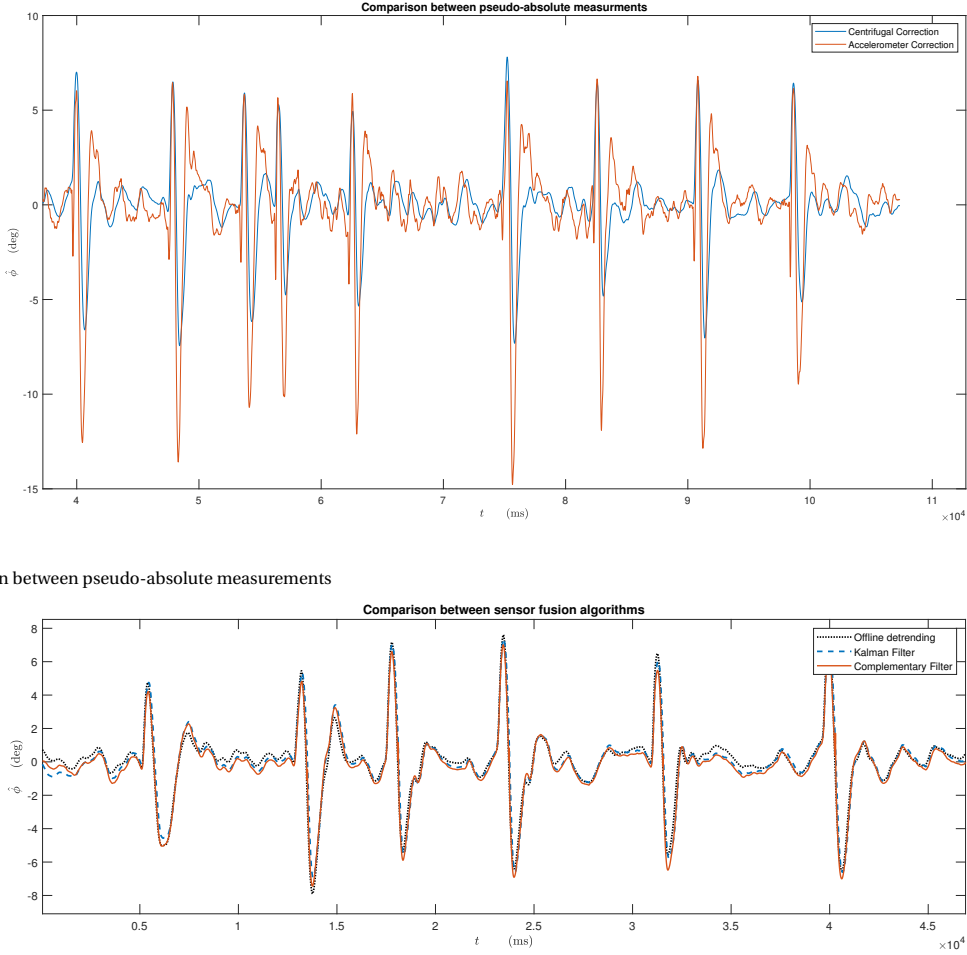
where W is the weighting function, $\hat{\phi}$ is the last available estimation of roll and $\bar{\phi}^2$ is a constant that can be used to adjust the weighting function. Sanjuro et al. used $\bar{\phi}^2 = 0.05$.

For the sensor fusion algorithm both a simple complimentary filter and a Kalman filter were tested. The complementary filter works by combining the desirable low-frequency characteristics of the absolute measurements with the desirable high-frequency characteristics of the euler integration output.

$$\hat{\phi}_k = (1 - \alpha) \cdot (\hat{\phi}_{k-1} + {}^B\omega_{x,k} \cdot dt) + \alpha \cdot \phi_m \quad (\text{B.9})$$

where k is the current iteration of the microcontroller and α is a constant, such that $0 < \alpha < 1$. The larger the α , the more pseudo absolute measurements are 'trusted'. As α goes to zero the estimate is mainly based on the integration output.

On the other hand, Kalman filters are also often used as state estimators when multiple measurement sources need to be combined into a single more reliable one. Often the output of a model is combined with absolute measurements and an estimation of the state is made by dynamically weighting the two sources of information. In this case a simple plant model is created which has $\dot{\phi} \approx {}^B\omega_x$ as input and produces the roll angle of the next time step given the previous one. In order to account for biases in the angular rate sensor an extra



(a) Comparison between pseudo-absolute measurements

(b) Comparison between sensor fusion algorithms

Figure B.1: a) Comparison between pseudo-absolute measurements. Both sources were fused with the integration output via a Kalman filter. The blue line is the result of the measurements used by Sanjurjo et al. [10] while the orange line is the result of the estimation produced using the accelerometer equation (A.3). b) Comparison between sensor fusion algorithms. For reference the output of the offline linear regression detrending is shown as a black dotted line.

state b_x is added to the model. The complete formulation is given by :

$$\begin{bmatrix} \hat{\phi} \\ \hat{b}_x \end{bmatrix}_k^- = \begin{bmatrix} 1 & -dt \\ 0 & 1 \end{bmatrix} \begin{bmatrix} \hat{\phi} \\ \hat{b}_x \end{bmatrix}_{k-1}^+ + \begin{bmatrix} dt \\ 0 \end{bmatrix} {}^B\omega_{x,k-1} \quad (\text{B.10})$$

The results are shown in figure B.1. In figure B.1a it is visible that the naive implementation using the assumption that the accelerometer only registers the gravitational acceleration does not work. However, for the first few seconds after turning on the bike the assumption is correct and a good initial condition estimate can be extracted in order to use as initial condition in the sensor fusion algorithm of choice. As far as the sensor fusion algorithm is concerned the results are shown in figure B.1b. A complimentary filter with $\alpha = 0.0022$ is used, while for the Kalman filter the process covariance matrix and measurement variance were equal to:

$$Q_P = \begin{bmatrix} 9e^{-4} & 0 \\ 0 & 3e^{-4} \end{bmatrix} dt \quad (\text{B.11})$$

$$Q_S = 0.5 \quad (\text{B.12})$$

Additionally the initial covariance matrix was equal to zero which means that the filter at the start "trusts" the model output; the Euler integration output. As a reference the result from the linear regression detrending is

also presented. The graph indicates that both methods successfully approximate the reference result. Furthermore, it is clear that with this general system model, only a slight performance gain (if any) can be gained by using the Kalman filter. Additionally, the implementation of the complimentary filter is far simpler and consequently much less computationally expensive. Had the Kalman filter been implemented on a system where an accurate dynamic model was present, the Kalman filter would – in pretty much all cases – trump the simpler complimentary filter. For this reason the complimentary filter approach was chosen for the on-line implementation of roll estimation in the steer-by-wire bicycle, considering the limiting clock speed of microcontroller Teensy 3.6.

The above pseudo-absolute measurements can only be used to estimate the roll angle. However there is a way to extract an estimation of the yaw relative to the magnetic north by using the magnetometer sensor, which is also part of the IMU. This is similar to how modern smartphones can work as a compass. Similar to how an estimation of the roll angle was made by equating the accelerometer readings with reference position where the gravitational acceleration is completley aligned with the bike's z-axis, the same can be done by equating the magnetometer readings with the reference position of the bike's x axis pointing towards the magnetic north. The magnetometer in this reference position are

$$\mathbf{B}_{ref} = B \begin{pmatrix} \cos \zeta \\ 0 \\ \sin \zeta \end{pmatrix} \quad (B.13)$$

where B is the geomagnetic field strength and ζ is the angle of inclination of the geomagnetic field measured downwards from horizontal. Both values vary over the earth's surface. Detailed geomagnetic field maps are available from the World Data Center for Geomagnetism at <http://wdc.kugi.kyoto-u.ac.jp/igrf/>. Fortunately, both B and ζ cancel out in the final formulation of the estimator.

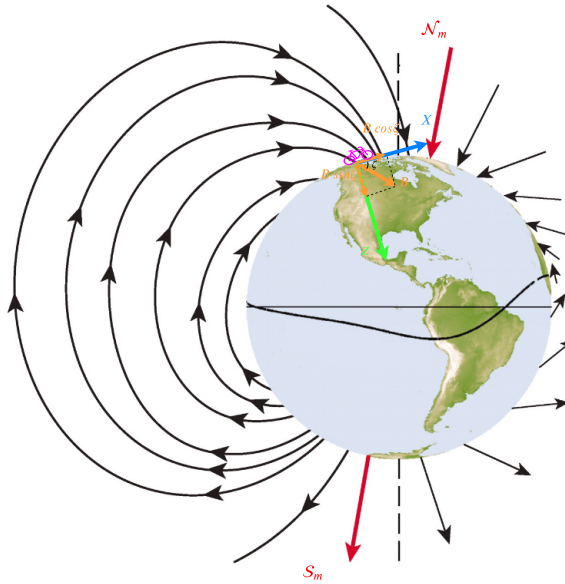


Figure B.2: Magnetic Field vectors in the reference position.

The measured magnetometer readings \mathbf{B}_p after three rotations are described by equations :

$$\mathbf{B}_p = \mathbf{R}_{xyz}(\phi, \theta, \psi) \cdot B \begin{pmatrix} \cos \zeta \\ 0 \\ \sin \zeta \end{pmatrix} + \begin{pmatrix} V_x \\ V_y \\ V_z \end{pmatrix} \quad (B.14)$$

where \mathbf{R}_{xyz} the rotation matrix defined in ??eq:rotmat2 and V_x, V_y, V_z are the components of the Hard-Iron vector, which is a fixed magnetic offset adding to the true magnetometer sensor output. The Hard-Iron offset is the sum of any intrinsic zero field offset within the magnetometer sensor itself plus permanent magnetic

fields within the PCB generated by magnetized ferromagnetic materials. It is quite normal for the Hard-Iron offset to greatly exceed the geomagnetic field. Therefore an accurate Hard-Iron estimation and subtraction are required.

The Hard-Iron offset can be estimated if we consider that the set of all 3d points defined by every magnetometer reading lies in the surface of a sphere with radius B . In the presence of the offset, the center of the sphere would be displaced by the Hard-Iron Vector \mathbf{V} . The components of vector \mathbf{V} can be estimated by fitting the magnetometer measurements to the equation:

$$(\mathbf{B}_p - \mathbf{V})^T (\mathbf{B}_p - \mathbf{V}) = B^2 \quad (\text{B.15})$$

Equation (B.15) was solved with the gradient descend method by minimizing the sum of the squared difference between the right and left hand side of the equation. The resulting Hard-Iron Offset Vecotor was :

$$\mathbf{V} = \begin{pmatrix} -22.03 & -26.14 & -1.651 \end{pmatrix} \quad [\mu\text{T}] \quad (\text{B.16})$$

In figure B.3 the locus defined by the set of vectors measured by the magnetometer is displayed. It is visible that after the correction the measurements lie on the surface of a sphere with center in the origin and radius approximately equal to 1 a.u.

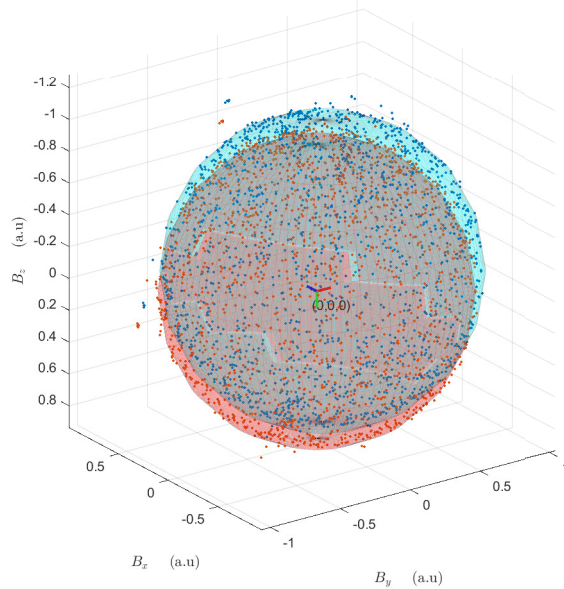


Figure B.3: The blue dots are the locus of the magnetometer readings before correcting for the hard iron offset. The red dots are the locus of the magnetometer readings after correcting for the offset. The magnetometer readings have been normalized so that 1 a.u= 49.0913 μT which is the Magnetic Field Intensity for the approximate location of TU Delft (Latitude 52° 0' 0" N and Longitude: 4° 22' 0" E).

Having estimated \mathbf{V} from equation (B.14) by assuming $\theta \approx 0$ we get :

$$\mathbf{B}_f = \mathbf{B}_p - \mathbf{V} = \mathbf{R}_x(\phi)\mathbf{R}_z(\psi) \cdot \begin{pmatrix} B \cos \zeta \\ 0 \\ B \sin \zeta \end{pmatrix} \quad (\text{B.17})$$

$$\mathbf{R}_x^T(\phi) \begin{pmatrix} B_{fx} \\ B_{fy} \\ B_{ fz} \end{pmatrix} = \begin{pmatrix} \cos \psi B \cos \delta \\ -\sin \psi B \cos \delta \\ B \sin \delta \end{pmatrix} \quad (\text{B.18})$$

$$\begin{pmatrix} B_{fx} \\ B_{fy} \cos \phi - B_{ fz} \sin \phi \\ B_{fy} \sin \phi + B_{ fz} \cos \phi \end{pmatrix} = \begin{pmatrix} \cos \psi B \cos \delta \\ -\sin \psi B \cos \delta \\ B \sin \delta \end{pmatrix} \quad (\text{B.19})$$

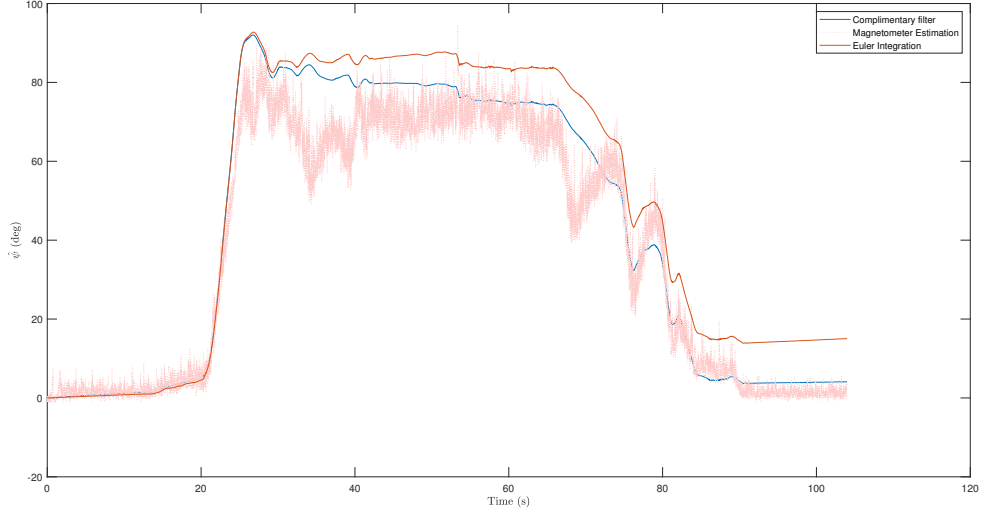


Figure B.4: Comparison of online yaw angle estimation. Red dotted line is the pure estimation from the magnetometer data. Orange line is the drifted euler integration output. Blue line is the result of the complimentary filter sensor fusing the other two signals. For the complimentary filter $a = 0.00027$.

By dividing the y and x component of equation (B.19) we get:

$$\hat{\psi} = \tan^{-1} \left(\frac{B_{fx} \sin \hat{\phi} - B_{fy} \cos \hat{\phi}}{B_{fz}} \right) \quad (\text{B.20})$$

where $\hat{\phi}$ is the estimate of roll angle obtained from the aforementioned methods. Equation (B.20) can now be used as a source of pseudo-absolute measurements for the sensor fusion algorithm of choice. Regarding signal fusion the same things apply as in the roll angle estimation case. Finally since we want the yaw angle relative to the starting position and not relative to the magnetic north the value of the first yaw estimation is subtracted from all subsequent computations.

BIBLIOGRAPHY

- [1] George Dialynas, Arend Schwab, and Riender Happee. Design and implementation of a steer-by-wire bicycle. 11 2018.
- [2] DJ Eaton. *Man-Machine Dynamics in the Stabilization of Single-Track Vehicles,* " Univ. of Michigan. PhD thesis, Ph. D. Thesis, 1975.
- [3] J. W. de Haan Georgios Dialynas. The response of the bicycle rider's body to vertical fore-and-aft and lateral perturbations; experimental tests. *Journal of Mechanical Engineering*, 463(2084):1955–1982, 2007.
- [4] JDG Kooijman and AL Schwab. A review on bicycle and motorcycle rider control with a perspective on handling qualities. *Vehicle system dynamics*, 51(11):1722–1764, 2013.
- [5] I. Krul, S. Nijman, and C. Stam. Verkeersongevallen 2016, 2016. URL <https://www.veiligheid.nl/organisatie/over-veiligheidnl/publicaties>.
- [6] Duane T McRuer and Ezra S Krendel. The human operator as a servo system element. *Journal of the Franklin Institute*, 267(5):381–403, 1959.
- [7] Duane T McRuer, Dunstan Graham, and Ezra S Krendel. Manual control of single-loop systems: Part i. *Journal of the Franklin Institute*, 283(1):1–29, 1967.
- [8] Duane T McRuer, Dunstan Graham, and Ezra S Krendel. Manual control of single-loop systems: Part ii. *Journal of the Franklin Institute*, 283(2):145–168, 1967.
- [9] Jaap P Meijaard, Jim M Papadopoulos, Andy Ruina, and Arend L Schwab. Linearized dynamics equations for the balance and steer of a bicycle: a benchmark and review. *Proceedings of the Royal society A: mathematical, physical and engineering sciences*, 463(2084):1955–1982, 2007.
- [10] Emilio Sanjurjo, Miguel A Naya, Javier Cuadrado, and Arend L Schwab. Roll angle estimator based on angular rate measurements for bicycles. *Vehicle System Dynamics*, pages 1–15, 2018.
- [11] AL Schwab and JDG Kooijman. Controllability of a bicycle. In *5th Asian Conference on Multibody Dynamics*, volume 6. Citeseer, 2010.